# Weak Electron–Phonon Coupling and Enhanced Thermoelectric Performance in n-type PbTe–Cu$_2$Se via Dynamic Phase Conversion

*Ming Wu, Hong-Hua Cui, Songting Cai, Shiqiang Hao, Yukun Liu, Trevor P. Bailey, Yinying Zhang, Zixuan Chen, Yubo Luo, Ctirad Uher, Christopher Wolverton, Vinayak P. Dravid, Yan Yu, Zhong-Zhen Luo,\* Zhigang Zou, Qingyu Yan,\* and Mercouri G. Kanatzidis\**

This study investigates Ga-doped n-type PbTe thermoelectric materials and the dynamic phase conversion process of the second phases via Cu$_2$Se alloying. Introducing Cu$_2$Se enhances its electrical transport properties while reducing its lattice thermal conductivity ($\kappa_{lat}$) via weak electron–phonon coupling. Cu$_2$Te and CuGa(Te/Se)$_2$ (tetragonal phase) nanocrystals precipitate during the alloying process, resulting in Te vacancies and interstitial Cu in the PbTe matrix. At room temperature, Te vacancies and interstitial Cu atoms serve as n-type dopants, increasing the carrier concentration and electrical conductivity from $\approx 1.18 \times 10^{19}$ cm$^{-3}$ and $\approx 1870$ S cm$^{-1}$ to $\approx 2.26 \times 10^{19}$ cm$^{-3}$ and $\approx 3029$ S cm$^{-1}$, respectively. With increasing temperature, the sample exhibits a dynamic change in Cu$_2$Te content and the generation of a new phase of CuGa(Te/Se)$_2$ (cubic phase), strengthening the phonon scattering and obtaining an ultralow $\kappa_{lat}$. Pb$_{0.975}$Ga$_{0.025}$Te-3%CuSe exhibits a maximum figure of merit of $\approx 1.63$ at 823 K, making it promising for intermediate-temperature device applications.

## 1. Introduction

Thermoelectric materials, which can collect and convert waste heat directly into electricity, can enhance energy utilization and efficiency. The dimensionless thermoelectric figure of merit ($ZT$) quantifies the efficiency of thermoelectric materials as $ZT = \sigma S^2 T/(\kappa_{ele} + \kappa_{lat})$, where $\sigma$, $S$, $T$, $\kappa_{ele}$, and $\kappa_{lat}$ represent the electrical conductivity, Seebeck coefficient, working temperature (K), and electronic and lattice thermal conductivity, respectively.[1] To maximize thermoelectric performance, an ideal thermoelectric material must possess a high power factor ($PF = \sigma S^2$), and a low total thermal conductivity ($\kappa_{tot} = \kappa_{ele} + \kappa_{lat}$). However, $\sigma$, $S$, and $\kappa_{ele}$ are strongly coupled and intertwined with the carrier

M. Wu, Z. Chen, Y. Yu, Z.-Z. Luo, Z. Zou
Key Laboratory of Eco-Materials Advanced Technology
College of Materials Science and Engineering
Fuzhou University
Fuzhou 350108, P. R. China
E-mail: zzluo@fzu.edu.cn

H.-H. Cui
Mechanical and Electrical Engineering Practice Center
Fuzhou University
Fuzhou 350108, P. R. China

S. Cai, Z.-Z. Luo, M. G. Kanatzidis
Department of Chemistry
Northwestern University
Evanston, IL 60208, USA
E-mail: m-kanatzidis@northwestern.edu

S. Cai, S. Hao, Y. Liu, C. Wolverton, V. P. Dravid
Department of Materials Science and Engineering
Northwestern University
Evanston, IL 60208, USA

T. P. Bailey, Y. Zhang, C. Uher
Department of Physics
University of Michigan
Ann Arbor, MI 48109, USA

Y. Luo
State Key Laboratory of Materials Processing and Die & Mould Technology
School of Materials Science and Engineering
Huazhong University of Science and Technology
Wuhan 430074, P. R. China

Y. Yu, Z.-Z. Luo, Z. Zou
Fujian Science & Technology Innovation Laboratory for Optoelectronic Information of China
Fuzhou, Fujian 350108, P. R. China

Y. Yu, Z.-Z. Luo
Key Laboratory of Advanced Materials Technologies
International (HongKong Macao and Taiwan) Joint Laboratory on Advanced Materials Technologies
College of Materials Science and Engineering
Fuzhou University
Fuzhou, Fujian 350108, P. R. China

Z.-Z. Luo, Q. Yan
School of Materials Science and Engineering
Nanyang Technological University
Singapore 639798 Singapore
E-mail: AlexYan@ntu.edu.sg

Z. Zou
Eco-Materials and Renewable Energy Research Center
College of Engineering and Applied Sciences
Nanjing University
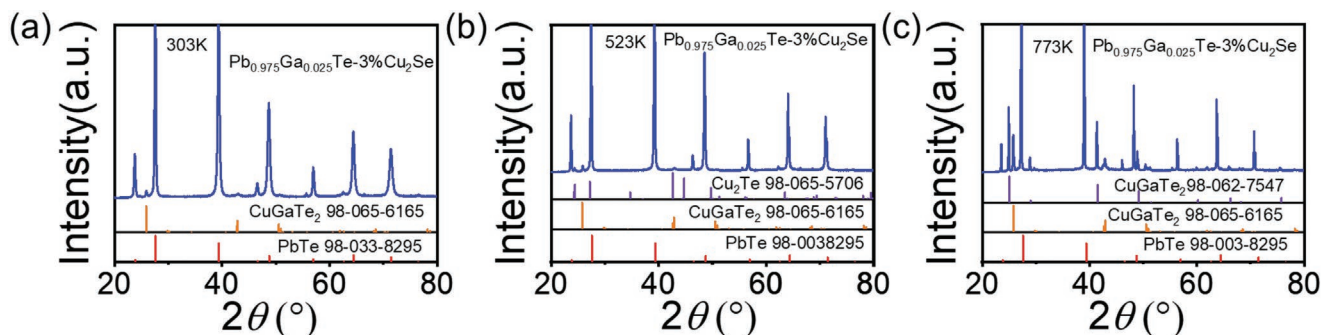Nanjing 210093, P. R. China

ADVANCED
SCIENCE NEWS
www.advancedsciencenews.com

ADVANCED
ENERGY
MATERIALS
www.advenergymat.de

**Figure 1.** In situ PXRD data of $Pb_{0.975}Ga_{0.025}Te-3\%Cu_2Se$ sample with the at a) 303 K, b) 523 K, and c) 773 K. The $CuGaTe_2$ 98-065-6165 belongs to a tetragonal phase with space group $I\bar{4}2d$, $a = 6.0235(1)$ Å, $c = 11.9398(0)$ Å, $V = 433.20(1)$ Å$^3$. The $Cu_2Te$ 98-065-5706 crystallizes in the space group $P6/mmm$ with $a = 4.237$ Å, $c = 7.274$ Å, $V = 113.09$ Å$^3$. The $CuGaTe_2$ 98-062-7547 is a cubic phase with the space group $F\bar{4}3m$, $a = 6.1639$ Å, $V = 234.18$ Å$^3$.

concentration ($n$). More carriers, for example, result in higher $\sigma$ ($\sigma = e\mu n$); $\kappa_{ele}$ is governed by the Wiedemann–Franz relation ($\kappa_{ele} = L\sigma T$, where $L$ represents the Lorenz number);[2] and $S$ is inversely proportional to $n$.[3] Therefore, decoupling the negatively correlated parameters is a primary goal for enhancing the $ZT$ value.

A new generation of PbTe-based materials has exceptional p-type performance with $ZT \approx 2.5$ as the only commercially available intermediate temperature range thermoelectric material.[4] However, advanced devices lag behind partly[5] because the $ZT$ for n-type PbTe is much lower due to the single conduction band (CB) structure versus the unique two-valence band (VB) structure for the p-type counterpart.[6] Importantly, p- and n-type PbTe materials are required for module fabrication for the practical application of thermoelectric technology.[5,7] Recently, effective approaches such as electronic band structure modulation (including midgap states via Ga doping and Ge alloying,[8] deep defect level via In doping,[9] shallow and deep level donor states via Ga doping,[10] and band flattening,[11] etc.) and phonon scattering manipulations (including multiphase nanostructures,[6] dislocations,[12] discordant off-center behavior,[1h,13] and dual-site point defects,[14] etc.) have been adopted to investigate the high performance n-type PbTe.

Previous research revealed that Ga doping can effectively increase the $S$ via introducing midgap states in the bandgap of PbTe,[8,10] when compared to conventional n-type dopants including I,[15] Sb,[16] Bi,[16] and La.[17] In contrast, Cu atoms have been demonstrated to fill the intrinsic Pb vacancies to improve carrier mobility ($\mu_H$) and induce local disorder and to form nanoscale and microscale Cu-rich precipitates, thereby reducing $\kappa_{lat}$.[18] Moreover, Cu atoms can form sub-nanostructure defects in the PbTe or SnTe[19] matrix as interstitials, resulting in locally disordered matrix lattices with sizes comparable to the phonon mean free path (0.1–10 nm) but much smaller than the PbTe carrier mean free path (100–1000 nm).[20] Therefore, these sub-nanostructure defects are beneficial for scattering phonons and maintaining electron mobility in the matrix.

In this study, we demonstrated that $Cu_2Te$ and $CuGa(Te/Se)_2$ (tetragonal phase) nanocrystals precipitated in Ga-doped

n-type PbTe with $Cu_2Se$ alloying, resulting in the formation of Te vacancies and interstitial Cu and an increase in $n$. The content of the $Cu_2Te$ second phase increased with increasing temperature, as measured using powder X-ray diffraction (PXRD). Moreover, the $Cu_2Te$ second phase disappeared and the $CuGa(Te/Se)_2$ (cubic phase) appeared above 773 K. The dynamic phase conversion causes a significant reduction in $\kappa_{lat}$. As a result of the synergistically increased $\sigma$ (from $\approx$1870 S cm$^{-1}$ for $Pb_{0.975}Ga_{0.025}Te$ to $\approx$3029 S cm$^{-1}$ for $x = 3$) and $\mu_H$, and the suppressed $\kappa_{lat}$ (from $\approx$1.70 W m$^{-1}$ K$^{-1}$ for $x = 0$ to $\approx$1.36 W m$^{-1}$ K$^{-1}$ for $x = 3$ samples) via weakened electron–phonon coupling, a maximum $ZT$ of $\approx$1.63 at 823 K can be obtained in $Pb_{0.975}Ga_{0.025}Te-3\%Cu_2Se$.

## 2. Results And Discussion

### 2.1. Structural Characterization

The PXRD patterns of the $Pb_{0.975}Ga_{0.025}Te-x\%Cu_2Se$ ($x = 0, 1, 2, 3, 4,$ and 5) samples at room temperature are shown in Figure S1 (Supporting Information). With a space group of $Fm\bar{3}m$, all of the main peaks can be well indexed to the PbTe phase (JCPDS 78-1905). Furthermore, the tetragonal $CuGa(Te/Se)_2$ phase (T-phase, $I\bar{4}2d$, $a = 6.0235$ Å, $c = 11.9398$ Å, $V = 433.20$ Å$^3$), became apparent with increasing $Cu_2Se$ content, as indicated by the two red stars, which is consistent with the extremely low solid solubility of Cu in the PbTe matrix (Figure S2, Supporting Information). However, Xiao et al. reported that the I-doped $PbTe-x\%Cu_2Te$ samples exhibited no second phases with $x < 5.5\%$.[18] The peaks shifted to a high-angle direction, indicating a solid solution of Se and Te, as confirmed by PXRD patterns of $CuGaTe_{2-x}Se_x$ (Figure S3, Supporting Information) and EDS mappings (discussed later). The lattice parameters gradually decrease with increasing $Cu_2Se$ content due to Cu$^+$ (0.96 Å) and Se$^{2-}$ (1.98 Å) substitutions at Pb$^{2+}$ (1.20 Å) and Te$^{2-}$ (2.21 Å) sites, respectively (Figure S4, Supporting Information).

Temperature-dependent PXRD was used to investigate the dynamic doping effect of Cu. The content of the $Cu_2Te$ second phase increased and was detected at $T > 473$ K, as shown in Figure S5 (Supporting Information). Furthermore, the $Cu_2Te$ phase disappeared, and the cubic $CuGaTe_2$ phase (C-phase, $F\bar{4}3m$, $a = 6.1639$ Å, $V = 234.18$ Å$^3$) appeared above 773 K, as

Q. Yan
Institute of Materials Research and Engineering
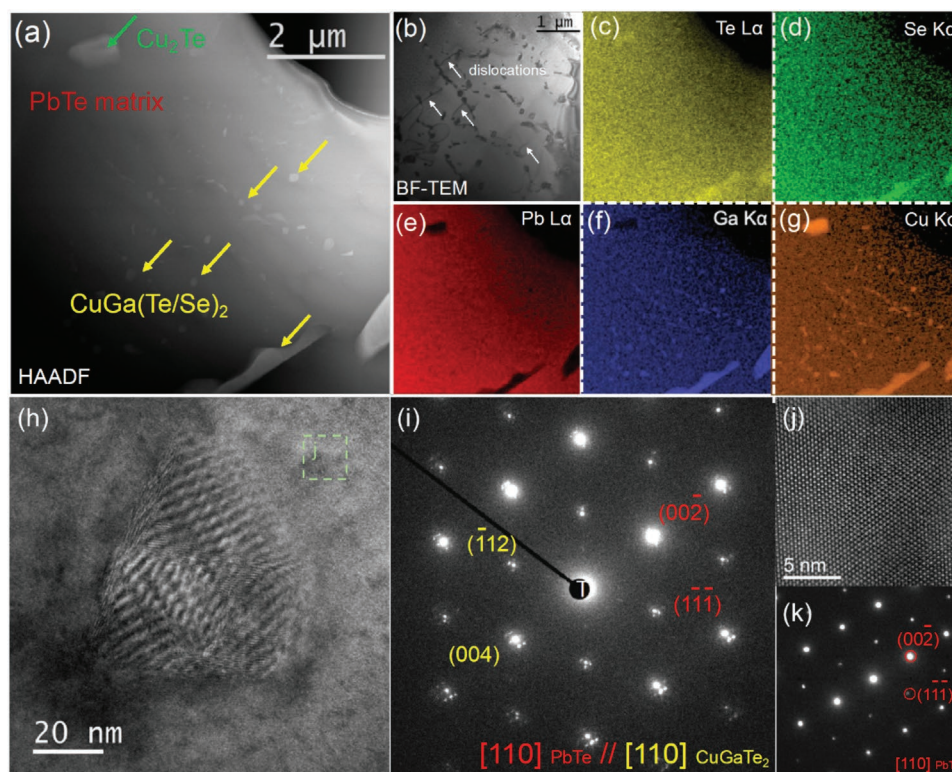A*STAR, Singapore 138634, Singapore

**2203325** (2 of 9)

**ADVANCED
SCIENCE NEWS**

www.advancedsciencenews.com

**ADVANCED
ENERGY
MATERIALS**

www.advenergymat.de

**Figure 2.** S/TEM analyses of $Pb_{0.975}Ga_{0.025}Te$-3%$Cu_2Se$ before the performance characteristics. a) High angle annular dark-field image and c–g) it is corresponding EDS mappings. b) Bright-field TEM image of a partial area of (a). h) High-resolution TEM (HREM) image of a typical coherent nano-precipitate $CuGaTe_2$ sitting in the PbTe matrix. i) Selected area electron diffraction (SAED) pattern of (h). j) Zoom-in version of the PbTe matrix part in h). k) SAED pattern in the area of (j).

shown in **Figure 1**. According to the conservation of Cu atoms, Equation (1) can be expressed as follows

$$Cu_2Se \rightarrow x\%Cu_2Se\,(in\,matrix)$$
$$+ y\%CuGa\,(Te\,/\,Se)_2\,(T-and\,C-phase) \quad (1)$$
$$+ z\%Cu_2Te$$
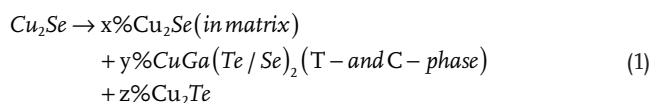
where x + 2y + z = 1.

The dissolution of $Cu_2Se$ in the PbTe matrix produces Te vacancies. The $CuGa(Te/Se)_2$ (T- and C-phase) phases can introduce interstitial Cu into the matrix simultaneously. The Te vacancy and interstitial Cu increase $n$ and $\sigma$. In contrast, the dynamic phase transition, point defects, nano- and microsized $Cu_2Te$, and $CuGa(Te/Se)_2$ are beneficial for phonon scattering. The details are discussed later in this study.

## 2.2. Microstructural Analysis and Nanostructuring

S/TEM was used on the $Pb_{0.975}Ga_{0.025}Te$-3%$Cu_2Se$ sample to investigate the all-scale microstructure and its relationship to the change in transport properties. **Figure 2**a shows a typical high-angle annular dark field image of the specimen, which shows a significant amount of nanosized (10–200 nm) and micrometer-sized precipitates embedded in the matrix with bright contrast/high Z-contrast. According to the corresponding EDS mapping (Figure 2c–g), the second phases are rich in Cu,

Ga, and Se. In contrast, they were deficient in Pb, as indicated using yellow arrows in Figure 2a, which were assigned to $CuGa(Te/Se)_2$. We also discovered several precipitates that were high in Cu and Te but low in Pb and Ga, as indicated using the green arrows, which was assigned to $Cu_2Te$. The quantitative EDS analysis results of three typical regions (PbTe matrix, $CuGa(Te/Se)_2$, and $Cu_2Te$) are shown in Figure S7 (Supporting Information). It is worth noting that the $Cu_2Te$ phases can only be found at grain boundaries; due to their small volume fraction in the sample, PXRD cannot detect signals from them. Figure 2b shows a bright-field TEM image of the specimen with mostly diffraction contrast, revealing a large number of dislocations around the nanoprecipitates, adding more scattering centers to the system.

A high-resolution TEM (HREM) image of a faceted nano precipitate embedded in a PbTe matrix is shown in Figure 2h. Along the [110] zone axis, the corresponding selected area electron diffraction (SAED) pattern from the matrix part belongs to the rock-salt PbTe phase ($Fm\bar{3}m$). Because of the coherency and lattice misfit between the two phases, translational Moiré fringes exist in the precipitate. Figure 2i depicts the corresponding SAED pattern. The bright spots in the PbTe matrix are highlighted in red along the [110] zone axis. Satellite spots were discovered around every PbTe spot, with the brightest spots indexed to the tetragonal $CuGaTe_2$ phase ($I\bar{4}2d$) along the [110] zone axis. In this direction, the atomic planes of the two phases were perfectly aligned, with
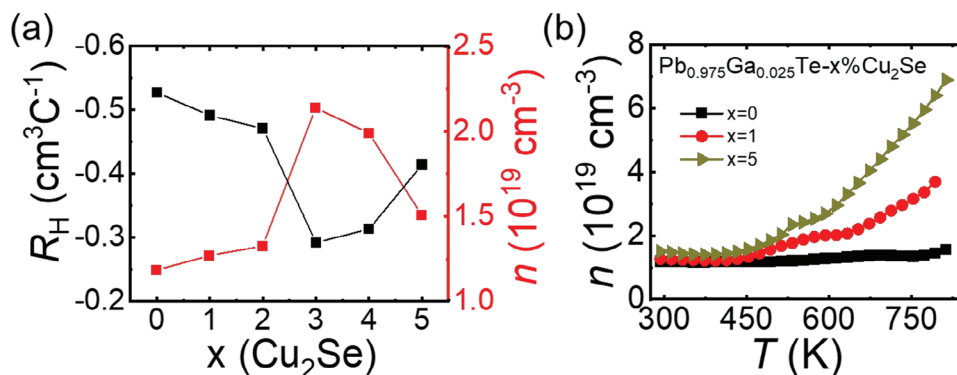
**ADVANCED
SCIENCE NEWS**
www.advancedsciencenews.com

**ADVANCED
ENERGY
MATERIALS**
www.advenergymat.de

**Figure 3.** a) Hall coefficient, $R_H$ and Hall carrier concentration $n$ for $Pb_{0.975}Ga_{0.025}Te$-x%$Cu_2Se$ ($x = 0$, 1, 2, 3, 4, and 5) at room temperature and b) the temperature dependence of $n$ for $Pb_{0.975}Ga_{0.025}Te$-x%$Cu_2Se$ ($x = 0$, 1, and 5).

no rotation or twisting observed. The weaker spots from the satellites originate from the double diffraction between the two phases.

## 2.3. Charge Transport Properties

### 2.3.1. Hall Coefficient

According to the Hall measurements, the charge $n$ gradually increases up to 3% with the addition of $Cu_2Se$, then spikes before showing a downward trend (**Figure 3**a). As in n-type doping, the formation of the second CuGa (Te/Se)$_2$ (T-phase) phase results in Te vacancies in the PbTe matrix. The samples exhibited a degenerate semiconducting nature with a rapidly increasing $n$ as the temperature increased (Figure 3b), particularly for the $x = 5$ samples. At $T > 600$ K, the $n$ was more than twice that of the I-doped PbTe-x%$Cu_2Te$ samples.[18] The multiple inflection points in the temperature-dependent curves indicate competing doping mechanisms among the elemental components, namely Te, Cu, and Ga.

### 2.3.2. Electrical Conductivity

The temperature-dependent electrical conductivities of $Pb_{0.975}Ga_{0.025}Te$-x%$Cu_2Se$ ($x = 0$, 1, 2, 3, 4, and 5) are shown in **Figure 4**. All samples exhibited typical degenerate semiconductor behavior, with gradually decreasing $\sigma$ as temperature increased. Over the entire $T$ range, the $Cu_2Se$ alloyed samples outperformed the $Pb_{0.975}Ga_{0.025}Te$ samples in terms of $\sigma$. At room temperature, for example, the $\sigma$ increased significantly from ≈1870 S cm$^{-1}$ for $Pb_{0.975}Ga_{0.025}Te$ to ≈3092 S cm$^{-1}$ for the $x = 1$ sample. This represents ≈65% increase over the $Cu_2Se$-free sample. The improved $n$ values from ≈$1.18 \times 10^{19}$ (for $x = 0$) to ≈$1.27 \times 10^{19}$ cm$^{-3}$ (for $x = 1$) and the enhanced mobilities $\mu_H$ from ≈990 (for $x = 0$) to ≈1521 cm$^2$ V$^{-1}$ s$^{-1}$ (for $x = 1$) are consistent with the enhanced $\sigma$, as shown in Figure 4c,d. Although $Cu_2Se$ is a p-type semiconductor,[21] $n$ increases significantly. This is attributed to the formation of Te vacancies and interstitial Cu. However, as the $Cu_2Se$ fraction increases, the $\sigma$ decreases owing to a decrease in $\mu_H$ from ≈1521 (for $x = 1$) to ≈999 cm$^2$ V$^{-1}$ s$^{-1}$

(for $x = 5$). Furthermore, the $x = 5$ sample exhibited the lowest $\sigma$ of ≈2466 S cm$^{-1}$. Remarkably, there is a "hump" in the $\sigma$–$T$ plots for the $Cu_2Se$ alloyed samples at $T > 623$ K compared to $Pb_{0.975}Ga_{0.025}Te$. According to Equation (1), increasing $Cu_2Te$ reduces the total content of $Cu_2Se$ in the matrix and CuGa(Te/Se)$_2$ (T- and C-phases). Consequently, the value of $n$ decreases. Therefore, the abnormal signature of the "hump" for $n$ and $\sigma$ may result from competition between the previously mentioned decreased and increased $n$ caused using Ga$^+$ ionization (Figure S10, Supporting Information). Moreover, as $Cu_2Te$ disappears at $T > 773$ K, $n$ increases. The I-doped PbTe-x%$Cu_2Te$ samples, in contrast, lack the distinctive "hump" signature in $n$, $\sigma$, and $S$ (refer to Section 2.3.3).[18]

### 2.3.3. Seebeck Coefficients

The temperature-dependent $S$ of $Pb_{0.975}Ga_{0.025}Te$-x%$Cu_2Se$ ($x = 0$, 1, 2, 3, 4, and 5) samples is shown in Figure 4b. The negative $S$ agreed with the negative $R_H$ (Figure S9, Supporting Information), indicating n-type properties. Because of the increased $n$, the $Cu_2Se$ alloyed samples exhibit a lower absolute $S$ value (≈82.2–98.5 µV K$^{-1}$ at room temperature and ≈190.8–215.8 µV K$^{-1}$ at 873 K) than the $Pb_{0.975}Ga_{0.025}Te$ samples (130.4 µV K$^{-1}$ at room temperature and 252.4 µV K$^{-1}$ at 873 K). In particular, for $Cu_2Se$ alloyed samples, the $S$ gradually decreased with increasing $Cu_2Se$ up to 3% and then increased. Moreover, the $S$ exhibits a similar signature to the "hump" as $\sigma$ at $T > 623$ K for $Cu_2Se$ alloyed samples. The $S = \frac{8\pi^2 k_B^2}{3eh^2} m^* T \left( \frac{\pi}{3n} \right)^{2/3}$, where $k_B$, $e$, $h$, and $m^*$ represent the Boltzmann constant, electron charge, Plank constant, and density of states (DOS) effective mass, respectively, is consistent with the variation of $n$ caused by the new phase generation as mentioned above (Figure 3b). Furthermore, the $\sigma$ and $S$ were stable during thermal cycling with repeated heating–cooling measurements, exhibiting good repeatability (Figure S11, Supporting Information).

Figure 3e depicts Pisarenko plots for the $Pb_{0.975}Ga_{0.025}Te$-x%$Cu_2Se$ ($x = 0$, 1, 2, 3, 4, and 5) samples at room temperature. The green and purple curves represent theoretical values calculated by the single parabolic band model with DOS effective masses ($m^*$) of 0.3 $m_e$ and 0.2 $m_e$ ($m_e$ is the free
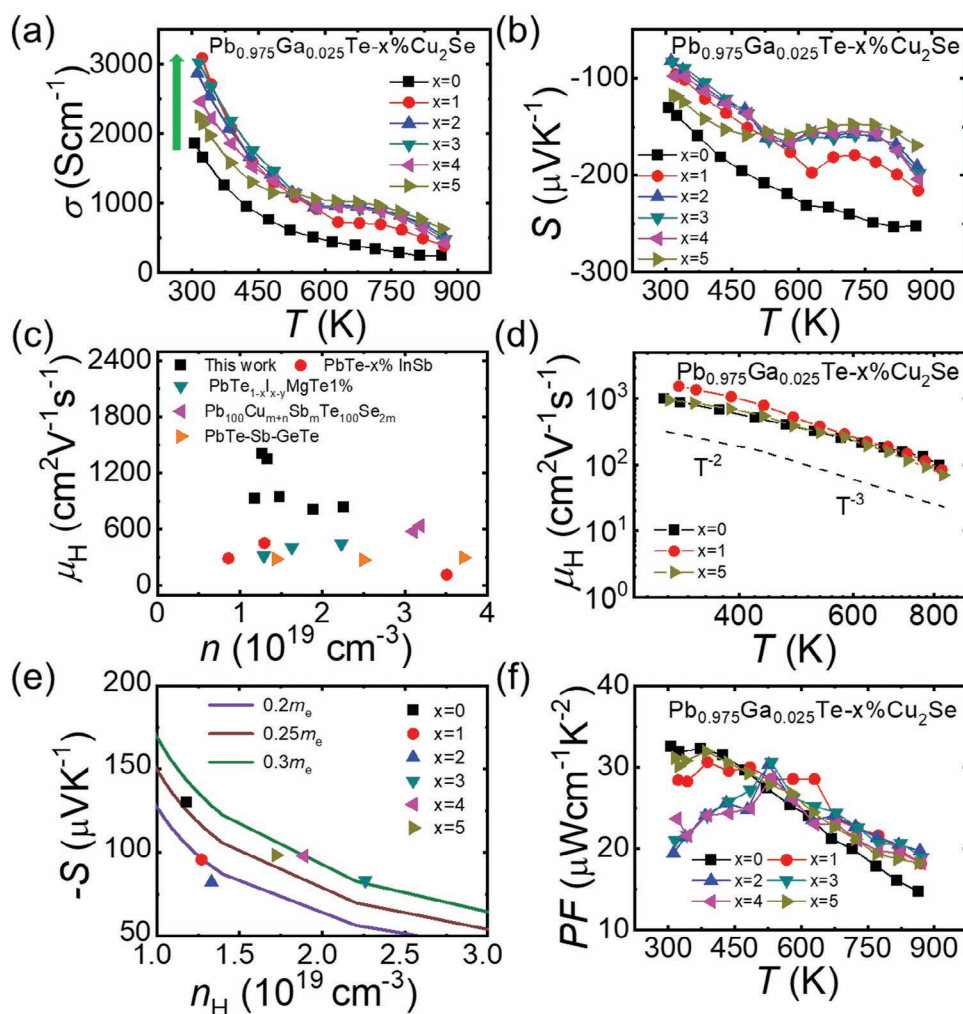
**ADVANCED**
**SCIENCE NEWS**

www.advancedsciencenews.com

**ADVANCED**
**ENERGY**
**MATERIALS**

www.advenergymat.de

**Figure 4.** Electronic properties as a function of temperature for $Pb_{0.975}Ga_{0.025}Te-x\%Cu_2Se$ ($x = 0, 1, 2, 3, 4,$ and 5). a) Electrical conductivity, $\sigma$; b) Seebeck coefficient, $S$; c) Comparison of carrier mobility, $\mu_H$, in this work with the known high performance n-type PbTe based samples.[6,22] d) Temperature-dependent $\mu_H$ for samples of $Pb_{0.975}Ga_{0.025}Te-x\%Cu_2Se$ ($x = 0, 1,$ and 5). e) Seebeck coefficient as a function of $n$ at room temperature. The solid curves in (e) are the theoretical Pisarenko curves for n-type PbTe with an effective mass of electrons of 0.2 $m_e$ (purple) and 0.3 $m_e$ (green); and f) Power Factor, $PF$.

electron mass), respectively. The $m^*$ decreases from ≈0.3 $m_e$ for $Pb_{0.975}Ga_{0.025}Te$ to less than 0.2 $m_e$ for $x = 2$ samples, then returns to 0.3 $m_e$ as the $Cu_2Se$ fraction increases. The lower $S$ resulted from the lighter $m^*$ and increased $n$, but the samples exhibited higher $\sigma$ and mobility than $Cu_2Se$ free samples (Figure 3).

### 2.3.4. Power Factor

The temperature-dependent $PF$s of $Pb_{0.975}Ga_{0.025}Te-x\%Cu_2Se$ ($x = 0, 1, 2, 3, 4,$ and 5) samples are shown in Figure 4f. Because of the low $S$ in the low-temperature range (300–523 K), the $Cu_2Se$ alloyed samples exhibited lower $PF$ than the parent material $Pb_{0.975}Ga_{0.025}Te$. However, at $T > 523$ K, they exhibit superior $PF$s due to their higher $\sigma$. $Pb_{0.975}Ga_{0.025}Te-3\%Cu_2Se$, for example, exhibits a high value of ≈19.0 $\mu W\ cm^{-1}\ K^{-2}$, which is ≈30% higher than the $Cu_2Se$ free sample $Pb_{0.975}Ga_{0.025}Te$ (≈14.7 $\mu W\ cm^{-1}\ K^{-2}$) at 873 K.

### 2.3.5. Thermal Conductivity

The temperature-dependent total thermal conductivities ($\kappa_{tot}$) for the $Pb_{0.975}Ga_{0.025}Te-x\%Cu_2Se$ ($x = 0, 1, 2, 3, 4,$ and 5) samples are higher than those of the $Cu_2Se$ free sample, as shown in **Figure 5**, due to the significant contribution from the increased $\kappa_{ele}$ at $T < 773$ K. For the $x > 1$ sample, there is a small flat region in the $\kappa_{tot}–T$ plot from 573 to 723 K. With increasing temperature, $Pb_{0.975}Ga_{0.025}Te-4\%Cu_2Se$ achieves the lowest $\kappa_{tot}$ of ≈1 W m$^{-1}$ K$^{-1}$ at 873 K.

To clarify the contributions of $\kappa_{ele}$ and $\kappa_{lat}$ in $Pb_{0.975}Ga_{0.025}Te-x\%Cu_2Se$, the $\kappa_{ele}$ is evaluated using the Wiedemann–Franz law, $\kappa_{ele} = L\sigma T$, where $L$ represents the Lorenz number calculated using the relationship: $L = (1.5 + \exp[-|S|/116]) \times 10^{-8}$ V$^2$ K$^{-2}$.[2] The $L$ and $\kappa_{ele}$ of $Pb_{0.975}Ga_{0.025}Te-x\%Cu_2Se$ are shown in Figure S11 (Supporting Information). The $Pb_{0.975}Ga_{0.025}Te-x\%Cu_2Se$ samples displayed a much higher $\kappa_{ele}$ than that of $Pb_{0.975}Ga_{0.025}Te$ over the entire measured temperature range, indicating that $Cu_2Se$ alloying

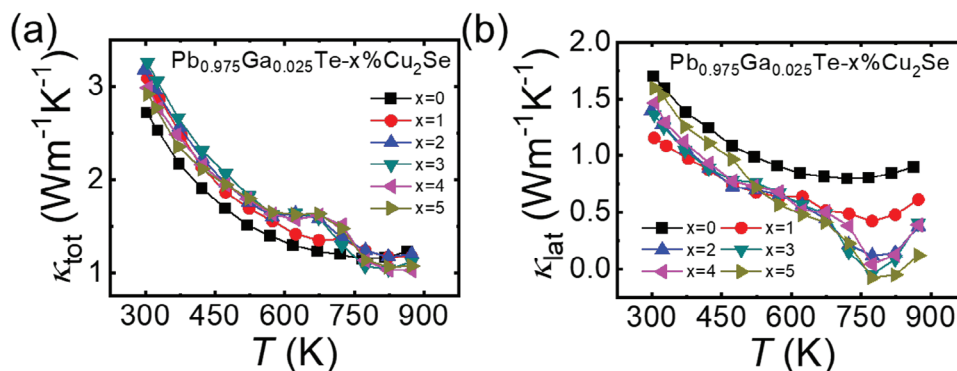**Figure 5.** Thermal properties as a function of temperature for $Pb_{0.975}Ga_{0.025}Te$-x%$Cu_2Se$ (x = 0, 1, 2, 3, 4, and 5). a) Total thermal conductivity, $\kappa_{tot}$ and (b) lattice thermal conductivity, $\kappa_{lat}$.

significantly enhanced $\sigma$. Furthermore, $\kappa_{ele}$ exhibits the "hump" at $T > 623$ K.

The $\kappa_{lat}$ of $Pb_{0.975}Ga_{0.025}Te$-x%$Cu_2Se$ was calculated using the formula $\kappa_{lat} = \kappa_{tot} - \kappa_{ele}$, and is shown in Figure 5b. Over the entire $T$ range, the $\kappa_{lat}$ values of the $Cu_2Se$ alloyed samples were significantly lower than those of $Pb_{0.975}Ga_{0.025}Te$. At room temperature, $\kappa_{lat}$ for the $x = 1$ sample was drastically reduced from $\approx 1.70$ Wm$^{-1}$ K$^{-1}$ for $x = 0$ to $\approx 1.15$ Wm$^{-1}$ K$^{-1}$ ($\approx 32\%$ reduction). The $\kappa_{lat}$ of $x > 2$ samples exhibited anomalous behavior at high temperatures, reaching an ultralow value of $\approx 0.05$ Wm$^{-1}$ K$^{-1}$ at 773 K. This value is significantly lower than the theoretical minimum $\kappa_{lat}$ value of $\approx 0.36$ Wm$^{-1}$ K$^{-1}$, as determined using the Debye–Callaway model.[23] As shown previously, the origin of the significantly reduced $\kappa_{lat}$ for the $Cu_2Se$ alloyed sample was systematically investigated using in situ PXRD and TEM. This abnormal $\kappa_{lat}$ was caused by weak electron–phonon coupling via dynamic phase generation, point defects, dislocations, nano- and microsized $Cu_2Te$ and $CuGa(Te/Se)_2$, and an overestimation of electronic component thermal conductivity governed by the Wiedemann–Franz law at temperatures above 673 K.[24] Although the $\kappa_{lat}$ value is difficult to evaluate precisely owing to the dynamic phase generation of $Cu_2Te$ and $CuGa(Te/Se)_2$ (C-phase), $\kappa_{tot}$ is veracious without that use of the Wiedemann–Franz law.
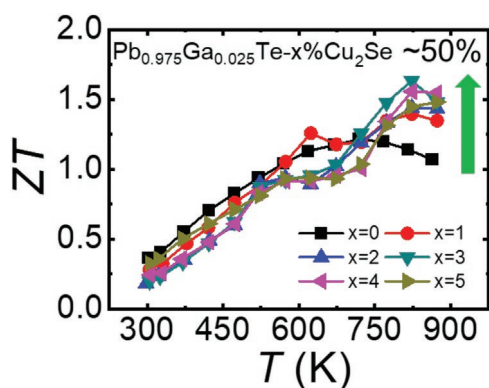
### 2.3.6. Figure of Merit

The $ZT$ value increased with temperature, peaked at $\approx 723$ K, and then dropped off for the $Cu_2Se$-free sample, as shown in **Figure 6**. However, for the $Cu_2Se$ alloyed samples, the $ZT$ values maintained a rising trend up to 823 K and obtained higher values. $Pb_{0.975}Ga_{0.025}Te$-3%$Cu_2Se$ sample has a peak $ZT$ of $\approx 1.63$ due to increased $PF$ and decreased $\kappa_{tot}$ in the high-temperature range ($T > 723$ K). $Cu_2Se$ alloy samples exhibit a higher $ZT$ than $Pb_{0.975}Ga_{0.025}Te$ and other high-performance n-type PbTe thermoelectrical materials.[25] Furthermore, an average $ZT$ ($ZT_{avg} = \frac{1}{T_H - T_C} \int_{T_C}^{T_H} ZTdT$) of $\approx 1.05$ from $T_C = 400$ K to $T_H = 823$ K was obtained for $Pb_{0.975}Ga_{0.025}Te$-3%$Cu_2Se$, which is one of the best $ZT_{avg}$ values for n-type PbTe.[11,26,27]

### 2.4. Density Functional Theory Calculations

We investigated the electronic band structure of $CuGaTe_2$ in PbTe to determine the dopant effect of $Cu_2Se$ in PbTe and Ga-doped PbTe, as the above experiments revealed the relevant precipitates of $Cu_2Te$ and $CuGaTe_2$. In addition to the strong alternating VBs, the CBs of Ga-doped and $Cu_2Te$ alloyed PbTe differ significantly from those of Ga-doped PbTe, as shown in **Figure 7**. Owing to the tervalent Ga substitution of Pb, the Ga 4s state contributes to a gap state across the Fermi level in Ga-doped PbTe. The Te 5p and Ga 4p states, in contrast, contributed to the DOS for the first CB minimum, as shown in Figure 7b. A critical effect for Ga-doped and $Cu_2Se$ alloyed PbTe is an increase in density of state effective mass to 0.40 $m_e$, which is greater than the corresponding n-type effective mass of PbTe, which is $\approx 0.26$ $m_e$.

To investigate the effects of Ga doping and $Cu_2Se$ alloying on the $\kappa_{lat}$ of PbTe, we calculated phonon dispersion for pure PbTe, Ga-doped PbTe, and Ga-doped and $Cu_2Se$ alloyed PbTe. The Cu, Ga, and Te atoms preferred to form a substitution Cu−Ga−Te complex (Figure S13a, Supporting Information) in the Ga-doped and $Cu_2Se$ alloyed PbTe, where the Cu and Ga atoms were the nearest neighbors. We calculated the decrease in $\kappa_{lat}$ after adding the Cu−Ga complex based on the phonon dispersion shown in **Figure 8**. $\kappa_{lat}$ of Ga-doped and $Cu_2Se$



**Figure 6.** Figure of merit ($ZT$) values for $Pb_{0.975}Ga_{0.025}Te$-x%$Cu_2Se$ (x = 0, 1, 2, 3, 4, and 5).

ADVANCED
SCIENCE NEWS
www.advancedsciencenews.com

ADVANCED
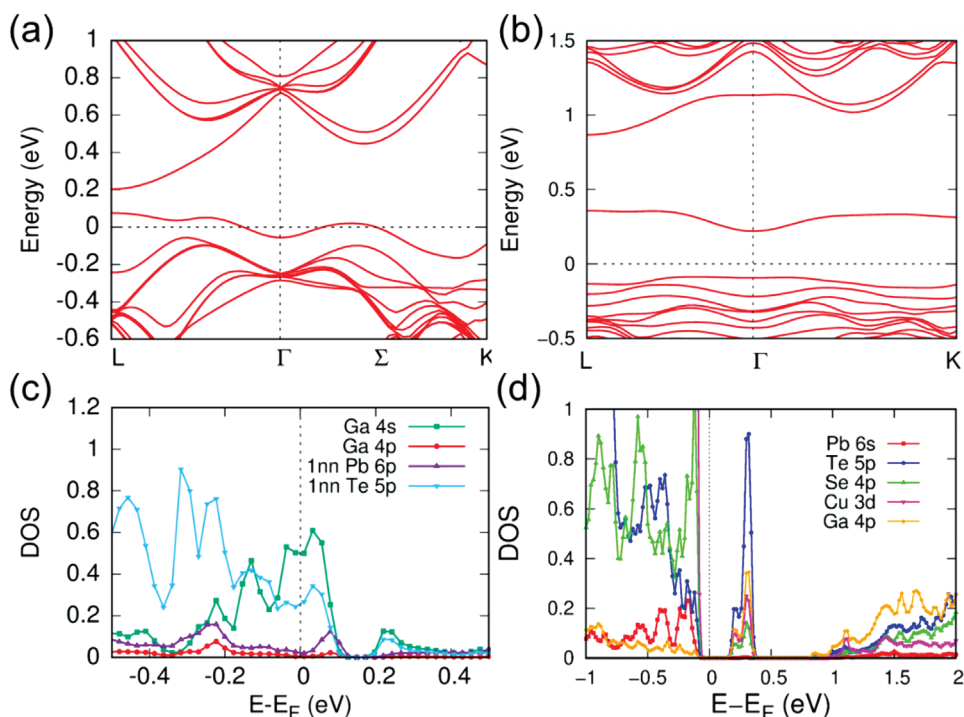ENERGY
MATERIALS
www.advenergymat.de

**Figure 7.** Electronic energy band structure of a) Ga-doped PbTe and c) Ga-doped and $Cu_2Se$-alloyed PbTe with the Ga off-centered model and corresponding projected density of states (b) and (d), respectively.

alloyed in PbTe exhibited a significant decrease, similar to the previous study involving Ga-doped and Zn-alloyed PbTe.[28] The Cu−Ga complex caused ≈35% reduction in $\kappa_{lat}$ at 300 K, as shown in Figure S13b (Supporting Information). This significant decrease could be attributed to several factors. Beyond the mass fluctuation of the Cu and Ga introduction, the calculated average phonon velocity LA branch of the Cu−Ga complex case (≈2750 ms$^{-1}$) was much lower than that of pure PbTe (3160 ms$^{-1}$). Moreover, the complex induced a relatively large local atomic strain, resulting in longer Pb−Te bond lengths than in the regular cases; therefore, relatively lower Pb vibration frequencies were induced. The low-frequency peaks of the Pb and Te projected phonon DOS (PDOS) are characterized by a left shift to a lower frequency, as shown in Figure 8b. Furthermore, in the case of the Cu−Ga complex, the Ga atom

generates low-frequency optical vibration modes, as shown at the G point with a frequency of ≈12 cm$^{-1}$. This model exhibited a small PDOS peak in the extremely low-frequency range (Figure 8b). This is attributed to the off-centered Cu−Ga atom, which results in a relatively loose atomic environment and, therefore, a significant $\kappa_{lat}$ reduction.

## 3. Conclusions

In summary, $Cu_2Se$ can enhance the electrical transport properties of PbTe, while also lowering the $\kappa_{lat}$ via dynamic phase generation. By introducing Te vacancies or interstitial Cu at room temperature, the $Cu_2Se$ in the PbTe matrix and the generated $CuGa(Te/Se)_2$ (T-phase) increased the $n$ and $\sigma$. With increasing
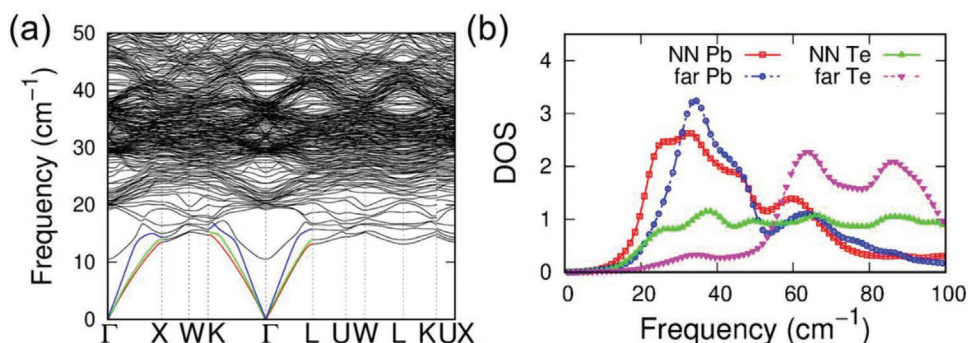


**Figure 8.** a) Phonon dispersion curves of Ga-doped and $Cu_2Se$ alloyed PbTe. b) The projected phonon density of states (PDOS) of Ga-doped and $Cu_2Se$ alloyed PbTe. "'NN Pb"' and "NN Te" stand for the Pb and Te atoms that are next nearest neighbors to the Cu−Ga−Se dopants and have longer Pb−Te bond lengths within the supercell, whereas "far Pb" and "far Te" are the regular cases.

temperature, the sample exhibited a dynamic change in $Cu_2Te$ content and the formation of new phases of $CuGa(Te/Se)_2$ (C-phase). Point defects, dislocations, $Cu_2Te$ and $CuGa(Te/Se)_2$ (T-phase) nanocrystals, dynamic phase generation of $Cu_2Te$ and $CuGa(Te/Se)_2$ (C-phase) intense phonon scattering and extremely low $\kappa_{lat} \approx 0.05$ Wm$^{-1}$ K$^{-1}$. PbTe is promising for intermediate-temperature device applications due to its maximum $ZT$ of $\approx 1.63$ at 823 K, which can be obtained for $Pb_{0.975}Ga_{0.025}Te$-3%$Cu_2Se$. A dynamic phase conversion is a novel approach that can be applied to various thermoelectric systems.

## 4. Experimental Section

*Raw Materials*: The following high-purity commercial reagents were used: Pb wire (99.99%, American Elements, USA); Te shot (99.999%, American Elements, USA); Ga shot (99.99%, Sigma-Aldrich, USA); Se shot (99.999%, Canada); and granular Cu (99.9%, Sigma-Aldrich, USA).

*Synthesis*: Stoichiometric compositions of $Pb_{0.975}Ga_{0.025}Te$-$x$%$Cu_2Se$ ($x$ = 0, 1, 2, 3, 4, and 5) were melted by mixing the raw materials in flame-sealed 13 mm diameter fused quartz tubes under a residual pressure of $\approx 2 \times 10^{-3}$ Torr. The tubes were heated to 1373 K for 11 h and then soaked for 6 h before being quenched to room temperature. The tubes were shaken gently at 1373 K to achieve homogeneous mixing. To prepare an $\approx 15$ g ingot of $Pb_{0.975}Ga_{0.025}Te$-3%$Cu_2Se$, the following amounts of raw materials were used: Pb (9 g, 43.44 mmol), Te (5.6846 g, 44.56 mmol), Ga (0.0777 g, 1.11 mmol), Se (0.1055 g, 1.34 mmol), and Cu (0.1699 g, 2.67 mmol).

*Hall Coefficient Measurements*: The Hall coefficient ($R_H$) was measured on samples with dimensions of $\approx 1 \times 3 \times 8$ mm$^3$ held in an Ar-filled sample probe within a homemade apparatus using an AC 4-probe method. A linear research AC resistance bridge (LR-700) operating at 17 Hz was used to measure the Hall resistance. The signal was modulated using excitation fields of $\pm 0.5$ Tesla provided by an air-bore Oxford superconducting magnet. The charge $n$ and $\mu_H$ were calculated as $n = 1/e|R_H|$ and $\mu_H = \sigma R_H$, respectively, where $e$ represents the electronic charge. Multiple measurements of the $R_H$ at fixed temperatures revealed $\approx 5\%$ uncertainty in $R_H$.

*Thermal Conductivity*: The thermal diffusivity ($D$) was measured directly on a Netzsch LFA457 with a continuous nitrogen flow using the laser flash analysis method. From the SPSed pellets, a square-shaped sample of $\approx 6 \times 6 \times 1.5$ mm$^3$ was cut and polished. To minimize emissivity errors, a thin layer of graphite spray coating was applied to squared sample surfaces. A Cowan model with pulse correction was used to analyze the $D$ data. $\kappa_{tot}$ was calculated using the expression $\kappa_{tot} = DC_p\rho$, where $C_p$ and $\rho$ represent the specific heat capacity and the density, respectively. The $C_p$ data were taken from a previous study.[29] The uncertainty of $D$ in this measurement was determined to be within 5%. $\rho$ was calculated as the mass of the samples divided by their volume. When all uncertainties from the $D$ measurement, $C_p$ calculation, and $\rho$ test are considered, the combined relative uncertainty for $ZT$ determination is $\approx 20\%$.

*Scanning/Transmission Electron Microscopy Characterization*: Scanning/transmission electron microscopy (S/TEM) and STEM energy dispersive spectroscopy (EDS) were performed on a JEOL ARM300F microscope set to 300 kV. The electron-beam transmitted transmission electron microscopy (TEM) specimens were prepared using conventional methods including cutting, grinding, and Ar-ion milling (2.8 kV for $\approx 0.5$ h until a hole is formed, followed by ion cleaning at 0.3 kV for 1 h) at a low temperature (liquid nitrogen stage).

*Electronic Band-Structure Calculations*: The relaxed geometries of various dopants in the PbTe host and the corresponding total energies were calculated using density functional theory (DFT) within the generalized gradient approximation of Perdew–Burke–Ernzerhof using the exchange-correlation functional with projector augmented wave potentials.[30] Periodic boundary conditions and a plane wave basis set were used, as implemented in the Vienna ab initio simulation package.[31] In all relaxation calculations, a basis set energy cutoff of 500 eV and a total energy numerical convergence criterion of $\approx 3$ meV per cation was adopted. For the $k$-point parameter, dense $k$-meshes with 4000 $k$-points per reciprocal atom in the Brillouin zone were used. For the Ga-doped and $Cu_2Se$ alloys, multiple configurations of one Cu and Ga substitution for two Pb atoms and Se substitution for Te in a $3 \times 3 \times 3$ PbTe supercell were first considered. For the band structure calculations, spin–orbit coupling is used to investigate the most energetically favorable configuration among the multiple possibilities.

*Lattice Vibration Calculations*: The frozen-phonon method was used to calculate the dynamical properties of relaxed structures.[32] The force-constant matrix is constructed using ab initio forces exerted on all cell atoms when a specific cell atom is slightly displaced from its equilibrium position. DFT calculations were performed with the VASP[33] code and the electronic exchange-correlation functional GGA-PBE.[30] Diagonalization of the corresponding dynamical matrix yielded the vibrational phonon modes. When compared to experiments with low-conductivity thermoelectric compounds, this method has recently been shown to produce accurate values of $\kappa_{lat}$.[28]

## Supporting Information

Supporting Information is available from the Wiley Online Library or from the author.

## Conflict of Interest

The authors declare no conflict of interest.

## Data Availability Statement

The data that support the findings of this study are available from the corresponding author upon reasonable request.

[1] a) K. F. Hsu, S. Loo, F. Guo, W. Chen, J. S. Dyck, C. Uher, T. Hogan, E. K. Polychroniadis, M. G. Kanatzidis, *Science* **2004**, *303*, 818; b) G. Tan, L.-D. Zhao, M. G. Kanatzidis, *Chem. Rev.* **2016**, *116*, 12123; c) T. Zhu, Y. Liu, C. Fu, J. P. Heremans, J. G. Snyder, X. Zhao, *Adv. Mater.* **2017**, *29*, 1605884; d) J. He, T. M. Tritt, *Science* **2017**, *357*, 1369; e) A. J. Minnich, M. S. Dresselhaus, Z. Ren, G. Chen, *Energy Environ. Sci.* **2009**, *2*, 466; f) G. J. Snyder, E. S. Toberer, *Nat. Mater.* **2008**, *7*, 105; g) Z.-Z. Luo, S. Hao, S. Cai, T. P. Bailey, G. Tan, Y. Luo, I. Spanopoulos, C. Uher, C. Wolverton, V. P. Dravid, Q. Yan, M. G. Kanatzidis, *J. Am. Chem. Soc.* **2019**, *141*, 6403; h) Z.-Z. Luo, S. Hao, X. Zhang, X. Hua, S. Cai, G. Tan, T. P. Bailey, R. Ma, C. Uher, C. Wolverton, V. P. Dravid, Q. Yan, M. G. Kanatzidis, *Energy Environ. Sci.* **2018**, *11*, 3220.

[2] H.-S. Kim, Z. M. Gibbs, Y. Tang, H. Wang, G. J. Snyder, *APL Mater.* **2015**, *3*, 041506.

[3] a) C. J. Vineis, A. Shakouri, A. Majumdar, M. G. Kanatzidis, *Adv. Mater.* **2010**, *22*, 3970; b) M. G. Kanatzidis, *Chem. Mater.* **2010**, *22*, 648; c) J. R. Sootsman, D. Y. Chung, M. G. Kanatzidis, *Angew. Chem., Int. Ed.* **2009**, *48*, 8616; d) Z.-Z. Luo, S. Cai, S. Hao, T. P. Bailey, X. Hu, R. Hanus, R. Ma, G. Tan, D. G. Chica, G. J. Snyder, C. Uher, C. Wolverton, V. P. Dravid, Q. Yan, M. G. Kanatzidis, *Chem. Mater.* **2019**, *31*, 5943.

[4] a) G. Tan, F. Shi, S. Hao, L.-D. Zhao, H. Chi, X. Zhang, C. Uher, C. Wolverton, V. P. Dravid, M. G. Kanatzidis, *Nat. Commun.* **2016**, *7*, 12167; b) Y. Wu, Z. Chen, P. Nan, F. Xiong, S. Lin, X. Zhang, Y. Chen, L. Chen, B. Ge, Y. Pei, *Joule* **2019**, *3*, 1276.

[5] Q. Yan, M. G. Kanatzidis, *Nat. Mater.* **2022**, *21*, 503.

[6] J. Zhang, D. Wu, D. He, D. Feng, M. Yin, X. Qin, J. He, *Adv. Mater.* **2017**, *29*, 1703148.

[7] G. Tan, M. Ohta, M. G. Kanatzidis, *Philos. Tr. Soc.* **2019**, *377*, 20180450.

[8] Z.-Z. Luo, S. Cai, S. Hao, T. P. Bailey, X. Su, I. Spanopoulos, I. Hadar, G. Tan, Y. Luo, J. Xu, C. Uher, C. Wolverton, V. P. Dravid, Q. Yan, M. G. Kanatzidis, *J. Am. Chem. Soc.* **2019**, *141*, 16169.

[9] Q. Zhang, Q. Song, X. Wang, J. Sun, Q. Zhu, K. Dahal, X. Lin, F. Cao, J. Zhou, S. Chen, G. Chen, J. Mao, Z. Ren, *Energy Environ. Sci.* **2018**, *11*, 933.

[10] X. Su, S. Hao, T. P. Bailey, S. Wang, I. Hadar, G. Tan, T. B. Song, Q. Zhang, C. Uher, C. Wolverton, *Adv. Energy Mater.* **2018**, *21*, 1800659.

[11] Y. Xiao, H. Wu, J. Cui, D. Wang, L. Fu, Y. Zhang, Y. Chen, J. He, S. J. Pennycook, L.-D. Zhao, *Energy Environ. Sci.* **2018**, *11*, 2486.

[12] a) Y. Xiao, Y. Wu, P. Nan, H. Dong, Z. Chen, Z. Chen, H. Gu, B. Ge, W. Li, Y. Pei, *Chem* **2020**, *6*, 523; b) Z. Chen, Z. Jian, W. Li, Y. Chang, B. Ge, R. Hanus, J. Yang, Y. Chen, M. Huang, G. J. Snyder, Y. Pei, *Adv. Mater.* **2017**, *29*, 1606768.

[13] a) J. M. Hodges, S. Hao, J. A. Grovogui, X. Zhang, T. P. Bailey, X. Li, Z. Gan, Y. Y. Hu, C. Uher, V. P. Dravid, C. Wolverton, M. G. Kanatzidis, *J. Am. Chem. Soc.* **2018**, *140*, 18115; b) Z.-Z. Luo, S. Cai, S. Hao, T. Bailey, Y. Luo, W. Luo, Y. Yu, C. Uher, C. M. Wolverton, V. Dravid, Z. Zou, Q. Yan, M. G. Kanatzidis, *Energy Environ. Sci.* **2022**, *15*, 368.

[14] L. Fu, M. Yin, D. Wu, W. Li, D. Feng, L. Huang, J. He, *Energy Environ. Sci.* **2017**, *10*, 2030.

[15] A. D. LaLonde, Y. Pei, G. J. Snyder, *Energy Environ. Sci.* **2011**, *4*, 2090.

[16] G. Tan, C. C. Stoumpos, S. Wang, T. P. Bailey, L.-D. Zhao, C. Uher, M. G. Kanatzidis, *Adv. Energy Mater.* **2017**, *7*, 1700099.

[17] Y. Pei, Z. M. Gibbs, A. Gloskovskii, B. Balke, W. G. Zeier, G. J. Snyder, *Adv. Energy Mater.* **2014**, *4*, 1400486.

[18] Y. Xiao, H. Wu, W. Li, M. Yin, Y. Pei, Y. Zhang, L. Fu, Y. Chen, S. J. Pennycook, L. Huang, J. He, L.-D. Zhao, *J. Am. Chem. Soc.* **2017**, *139*, 51.

[19] W. Li, L. Zheng, B. Ge, S. Lin, X. Zhang, Z. Chen, Y. Chang, Y. Pei, *Adv. Mater.* **2017**, *29*, 1605887.

[20] a) Y. Qin, Y. Xiao, L.-D. Zhao, *APL Mater.* **2020**, *8*, 010901; b) C. Zhou, Y. Yu, Y. K. Lee, O. Cojocaru-Mirédin, B. Yoo, S.-P. Cho, J. Im, M. Wuttig, T. Hyeon, I. Chung, *J. Am. Chem. Soc.* **2018**, *140*, 15535.

[21] H. Liu, X. Shi, F. Xu, L. Zhang, W. Zhang, L. Chen, Q. Li, C. Uher, T. Day, G. J. Snyder, *Nat. Mater.* **2012**, *11*, 422.

[22] a) P. Jood, M. Ohta, M. Kunii, X. Hu, H. Nishiate, A. Yamamoto, M. G. Kanatzidis, *J. Mater. Chem. C* **2015**, *3*, 10401; b) S. Wang, Y. Xiao, Y. Chen, S. Peng, D. Wang, T. Hong, Z. Yang, Y. Sun, X. Gao, L.-D. Zhao, *Energy Environ. Sci.* **2021**, *14*, 451; c) Z.-Z. Luo, X. Zhang, X. Hua, G. Tan, T. P. Bailey, J. Xu, C. Uher, C. Wolverton, V. P. Dravid, Q. Yan, M. G. Kanatzidis, *Adv. Funct. Mater.* **2018**, *28*, 1801617.

[23] Y. K. Koh, C. J. Vineis, S. D. Calawa, M. P. Walsh, D. G. Cahill, *Appl. Phys. Lett.* **2009**, *94*, 153101.

[24] X. Qian, D. Wang, Y. Zhang, H. Wu, S. J. Pennycook, L. Zheng, P. F. P. Poudeu, L.-D. Zhao, *J. Mater. Chem. A* **2020**, *8*, 5699.

[25] a) Y. Li, J. Zhang, Y. Pan, Y. Jiang, K. Wang, J. Yang, Y. Pei, Q. Zhu, M. T. Agne, G. J. Snyder, Z. Ren, W. Zhang, J. Luo, *Energy Environ. Sci.* **2019**, *12*, 3089; b) X. Yu, H. Wu, W. Li, M. Yin, Y. Pei, Y. Zhang, L. Fu, Y. Chen, S. J. Pennycook, L. Huang, J. He, L.-D. Zhao, *J. Am. Chem. Soc.* **2017**, *139*, 18732; c) Y. Han, Z. Chen, C. Xin, Y. Pei, M. Zhou, R. Huang, L. Li, *J. Alloys Compd.* **2014**, *600*, 91; d) X. Wang, X. Li, Z. Zhang, X. Li, C. Chen, S. Li, X. Lin, J. Sui, X. Liu, F. Cao, J. Yang, Q. Zhang, *Mater. Today Phys.* **2018**, *6*, 45; e) H. Liu, Z. Chen, J. Tang, Y. Zhong, X. Guo, F. Zhang, R. Ang, *ACS Appl. Mater. Interfaces* **2020**, *12*, 52952; f) H.-T. Liu, Q. Sun, Y. Zhong, C.-L. Xia, Y. Chen, X.-L. Shi, Z.-G. Chen, R. Ang, *Mater. Today Phys.* **2022**, *24*, 100677.

[26] a) M. Dutta, R. K. Biswas, S. K. Pati, K. Biswas, *ACS Energy Lett.* **2021**, *6*, 1625; b) L. You, J. Zhang, Y. Pan, Y. Jiang, K. Wang, J. Yang, Y. Pei, Q. Zhu, M. T. Agne, G. J. Snyder, Z. Ren, W. Zhang, J. Luo, *Energy Environ. Sci.* **2019**, *12*, 3089;

[27] P.-Y. Deng, K.-K. Wang, J.-Y. Du, H.-J. Wu, *Adv. Funct. Mater.* **2020**, *30*, 2005479;

[28] a) M. Asen-Palmer, K. Bartkowski, E. Gmelin, M. Cardona, A. P. Zhernov, A. V. Inyushkin, A. Taldenkov, V. I. Ozhogin, K. M. Itoh, E. E. Haller, *Phys. Rev. B* **1997**, *56*, 9431; b) Y. Zhang, E. Skoug, J. Cain, V. Ozoliņš, D. Morelli, C. Wolverton, *Phys. Rev. B* **2012**, *85*, 054306; c) D. T. Morelli, J. P. Heremans, G. A. Slack, *Phys. Rev. B* **2002**, *66*, 195304.

[29] R. Blachnik, R. Igel, *Z. Naturforsch., B* **1974**, *29*, 625.

[30] J. P. Perdew, K. Burke, M. Ernzerhof, *Phys. Rev. Lett.* **1996**, *77*, 3865.

[31] G. Kresse, J. Furthmüller, *Phys. Rev. B* **1996**, *54*, 11169.

[32] L. Chaput, A. Togo, I. Tanaka, G. Hug, *Phys. Rev. B* **2011**, *84*, 094302.

[33] G. Kresse, D. Joubert, *Phys. Rev. B* **1999**, *59*, 1758.